11th World Congress on Computational Mechanics (WCCM XI)
5th European Conference on Computational Mechanics (ECCM V)
6th European Conference on Computational Fluid Dynamics (ECFD VI)
E. Oñate, J. Oliver and A. Huerta (Eds)

MODELLING OF TIP VORTEX CAVITATION FOR ENGINEERING APPLICATIONS IN OPENFOAM

Joost J. A. Schot[1], Pepijn C. Pennings[1], Mathieu J. B. M. Pourquie[1], Tom J. C. van Terwisga[1]

[1]Technische Universiteit Delft: Fluid Mechanics Section (FM) at the Laboratory for Aero & Hydrodynamics, Mekelweg 2 2628 CD Delft, J.J.A.Schot@student.tudelft.nl, P.C.Pennings@tudelft.nl, M.J.B.M.Pourquie@tudelft.nl, T.J.C.vanTerwisga@tudelft.nl

Key words: Vortex cavitation, Elliptical planform, OpenFOAM, RANS, Transition, Rotation correction.

Abstract. In this paper modelling assumptions for the prediction of tip vortex flow and vortex cavitation with the RANS equations and homogeneous fluid approach in OpenFOAM are presented. The effects of the changes in the turbulence model are investigated and the results are compared with PIV measurements.

1 INTRODUCTION

Tip vortex cavitation has been studied extensively for a wing with an elliptical planform with an aspect ratio of 3 and a NACA $66_2 - 415$ cross-sectional shape using an $a = 0.8$ mean line [1]. It was found that at certain cavitation numbers the tip vortex cavity trailing from this wing emits a strong tonal noise, called vortex singing [2]. The cause of the singing behaviour of the vortex cavity is not yet known, but most likely related to excitement of one of its natural vibration modes, described by [3], due to flow instabilities in the tip region. This singing behaviour is of particular interest as it is one of the possible explanations of the high frequency broadband noise generated by skewed ship propellers, designed to avoid sheet cavitation [4].

The conventional modelling approach for cavitation problems in engineering applications is with a first order closure Reynolds averaged Navier-Stokes (RANS) model. The multi-phase aspects are included with the homogeneous fluid approach, the volume of fluid (VOF) method and a mass transfer model. It is known that most of these turbulence models need corrections in rotational flows. Other methods, such as a Reynolds Stress Transport Model (RSTM) or Large Eddy Simulations (LES) increase the computational time enormously, especially when the boundary layer needs to be resolved. Further complications arise when transition of the boundary layer is important, which is the case for the wing in the present study. Therefore, vortex cavitation is approximated with a

corrected RANS model which includes the damping effects of rotation and transition. The mass transfer rate for vortex cavitation is modelled as evaporation through an interface.

The accuracy of the chosen rotation correction and transition model for the Spalart-Allmaras turbulence model for the prediction of the tip vortex trailing the mentioned foil is studied and compared with preliminary results of PIV measurement performed in the cavitation tunnel of the TU Delft. Furthermore, the changes on the mean flow in the computations are investigated in the case were cavitation is present.

2 PHYSICAL MODEL

In the present study the conventional modelling assumptions for cavitation in engineering applications are extended to include the major effects associated with vortex cavitation. This includes changes to the turbulence model in order to account for the effects of transition and damping resulting from the high rotational velocity in the vortex core. Furthermore, the choice of the mass transfer model is important to represent the appropriate cavitation regime. It is observed that the vortex cavity at model scale is entirely filled with vapour, in contrast to the cloud of bubbles that is usually observed in the case of sheet cavitation.

The flow with cavitation is modelled as an incompressible mixture containing water and vapour. The interaction between the phases is modelled with the homogeneous fluid approach and Reynolds averaging is applied on the equations. This results in equation 1 for the conservation of mass and 2 for conservation of momentum. The assumptions of the homogeneous fluid approach lead to a mixture density and viscosity, given by $\rho = \phi_l \rho_l + (1 - \phi_l)\rho_v$ and $\mu = \phi_l \mu_l + (1 - \phi_l)\mu_v$. The Reynolds stress is modelled with the Boussinesq hypothesis resulting in $\mu_{eff} = \mu + \mu_t$. The surface tension is neglected, because it introduced numerical difficulties called spurious currents [5] which could only be avoided by using an infeasibly small time step.

$$\frac{\partial}{\partial t}\bar{\rho} + \nabla \cdot \bar{\rho}\tilde{U} = 0 \tag{1}$$

$$\frac{\partial}{\partial t}\bar{\rho}\tilde{U} + \nabla \cdot \left(\bar{\rho}\tilde{U}\tilde{U}\right) = -\nabla\left(\bar{p}\boldsymbol{I} + \frac{2}{3}\bar{\rho}k\boldsymbol{I}\right) + \nabla \cdot (2\mu_{eff}\tilde{\boldsymbol{S}}) \tag{2}$$

The turbulent viscosity is approximated with the Spalart-Allmaras (SA) model including trip terms used for transition and the damping of the turbulence due to high rotation proposed in [6]. Both extensions to the standard turbulence model are implemented in version 2.1.1 of OpenFOAM. For the standard formulation of the Spalart-Allmaras model with trip terms the reader is referred to [7]. The original production term of the model and the correction for rotation are given in equation 3 and 4 respectively.

The correction for the damping effects of rotation changes the component Ω of $\hat{S}$ shown in equation 3 of the production term $C_{b1}(1 - f_{t2})\hat{S}\tilde{\nu}$ in Ω^*. This introduces a damping rate depending on the empirical constant C_{rot} when the magnitude of the rate-of-rotation tensor exceeds the magnitude of the rate-of-strain tensor.

$$\begin{aligned} \hat{S} =& \Omega + \frac{\tilde{\nu}}{\kappa^2 d^2} f_{v2} \\ \Omega =& |2\tilde{\boldsymbol{\Omega}}| \end{aligned} \tag{3}$$

$$\Omega^* = \Omega + C_{rot} min(0, |2\tilde{\boldsymbol{S}}| - \Omega) \tag{4}$$

The Volume Of Fluid (VOF) method is used to track the interface (eqn. 5). The mass transfer rate is based on the Langmuir mass transfer rate through an interface and the area density of the interface is approximated with a global estimate of the local grid spacing (eqn. 6).

$$\frac{\partial \phi_l}{\partial t} + \nabla \cdot (\phi_l \tilde{U}) = \frac{1}{\rho_l} \Gamma_l \tag{5}$$

$$\Gamma_l = A_d \; C_{Langmuir} \; (p - p_v) \sim \frac{10^{-3}}{\Delta x} \; (p - p_v) \frac{kg}{m^3 s} \tag{6}$$

3 NUMERICAL MODEL

The numerical methods of OpenFOAM are used in this study, which applies the finite volume method to discretize the equations. The spatial accuracy is limited to second order, as a result of the approximation of the divergence term after applying Gauss' theorem which is of this order. Furthermore, no stable higher order schemes are included for the interpolation of the face values. This leads to a numerical viscosity of the order of the fluid viscosity for a study on the analytical Taylor-Green vortex with similar properties as the vortex trailing the wing in the present study [8].

The solver simpleFoam is used for the steady-state fully wetted computations. For the interpolation of the face values for the convective term of the momentum equation the 'linearUpwindV' scheme is used. For the face values for the convective term of the turbulence model the 'limitedLinear' scheme is used. Other face values are interpolated with the 'linear' scheme.

For the steady-state cavitating computations the interPhaseChangeFoam solver is applied with the same interpolation schemes. The temporal discretisation is performed with the local time stepping scheme of OpenFoam 'localEuler'. For the interpolation of the liquid fraction near the interface the 'SuperBee' scheme is used and the interface compression coefficient (C_λ) of OpenFOAM is set to 1. For the time step the advised maximum Courant number of 0.2 is used.

4 RESULTS

First the computational domain and grid are described. The transition is applied on a specified line approximated by transition locations predicted by xFoil at two locations along the span of the wing and the mid chord position at the tip. First fully wetted steady state computations are discussed with the Spalart-Allmaras model with rotation correction (SA-R) and the model with transition terms (SA-R-trip). Then the effects of cavitation are discussed, at a cavitation number of 1.7 which was chosen to avoid the presence of sheet cavitation.

4.1 Computational domain

The computational domain has the same dimensions as the test section of the cavitation tunnel at the TU Delft and is shown in figure 1. The wing has been set at a geometrical angle of attack (α_g) of 9 degrees, in order to avoid the difficulty of resolving the laminar separation bubble which forms at lower angles of attack. The chord length of the wing (c) is 125.6 mm. The half span ($\frac{1}{2}b$) is equal to 150 mm. The trailing edge has been cut off with a thickness of 0.3 mm. It should be noted that for the line plots shown later on a local coordinate system has been used.

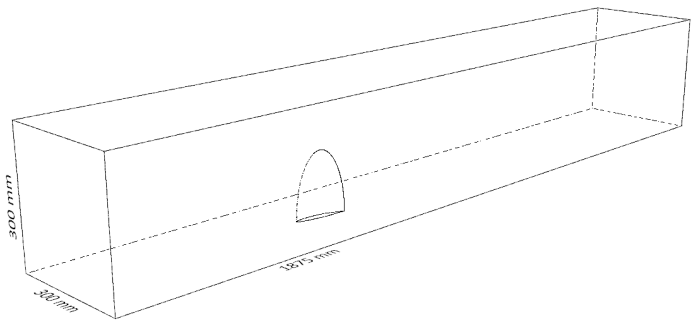

Figure 1: Computational domain, similar to the test section of the cavitation tunnel at the TU Delft. The flow is from left to right.

The test case was conducted at a Reynolds number of 6.8 10^5, which corresponds to an inlet velocity of 5.43 $\frac{m}{s}$. The kinematic viscosity is set to be $1.0034 \cdot 10^{-6} \frac{m^2}{s}$, which corresponds to fresh water at a temperature of 20° Celsius. The density of the liquid is $998.2 \frac{kg}{m^3}$ and the vapour pressure $2339.3Pa$ [9]. For the cavitating case the vapour density of $0.01731 \frac{kg}{m^3}$ and kinematic viscosity of $561.84 \cdot 10^{-6} \frac{m^2}{s}$ are used for water vapour at the same temperature at vapour pressure based on the IAPWS-IF97 table [10].

4.2 Computational grid

For the computations an unstructured grid has been generated with approximately 25 million cells with around 15 cells over the viscous core of the vortex for the fully turbulent

case. The case with a laminar boundary layer section has approximately 10 cells over the core. The grid near the root at the trailing edge and leading edge is shown in figure 2 and 3. The refinement near the vortex core at the tip is shown in figure 4. The boundary layer on the wing is fully resolved with a maximum y^+ value of around 2.

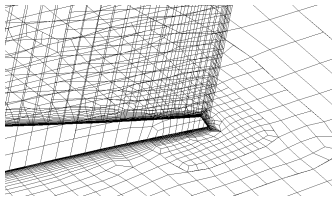

Figure 2: Grid refinement near the trailing edge at the root of the wing.

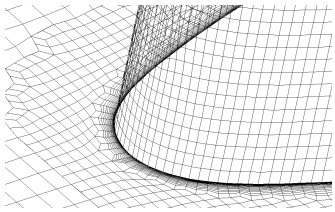

Figure 3: Grid refinement near the leading edge at the root of the wing.

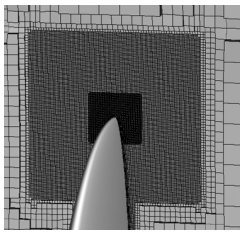

Figure 4: Grid refinement in the tip vortex region near the tip of the wing.

4.3 Surface flow pattern and integral quantities

First the flow over the wing is compared with experiments in figure 5 and 6. It is observed that for the case with early transition the general flow pattern agrees qualitatively with oil visualisation experiments [11], but a laminar separation bubble at lower angles of attack can not be reproduced.

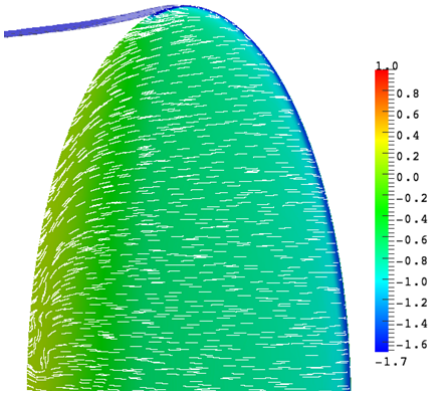

Figure 5: Pressure coefficient and surface streamlines based on the wall friction on the suction side computed with the SA-R model.

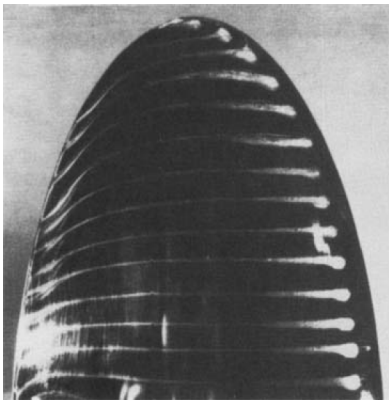

Figure 6: Oil visualization of surface streamlines with early transition at $\alpha_g = 10°$ and $Re = 5.3\ 10^5$ [11].

The result of the laminar separation bubble, which can still be present at $\alpha_g = 9°$ in experiments, is a decrease in the lift coefficient. This is visible in the experimental values in table 1. When the results are compared with thin airfoil theory based on the experimentally observed range of zero lift angles it shows agreement with the computations.

Table 1: Comparison of the predicted lift and drag coefficient with experiments.

	C_l	C_{d_i}	$C_d - C_{d_i}$
SA-R	0.72	0.055	0.010
SA-R-trip	0.74	0.058	0.007
Exp. [1]	0.64	0.043	0.033
Exp. TU Delft	0.56	-	-
Thin airfoil theory	0.71 ± 0.04	-	-

4.4 Effects of the rotation corrections

The turbulence production in the core of the vortex is damped by the correction to the SA model given in equation 4, referred to as the SA-R model. In figure 7 the effect on the production term in a cross section of the vortex is shown at one chord length downstream of the tip. It is observed that damping is present in the vortex core and the shear layer rolling up into it. The damping of the production is at a rate proportional to the empirical constant C_{rot} and isotropic. However, in turbulent vortices it is observed that mainly the radial turbulent fluctuations are damped [12] and not the other components.

The production of turbulence resulting from the gradient of the axial velocity is not present with this correction. This effect is shown in figure 8 where it can be seen that the production term is highly damped in the region where the gradient in axial velocity ($\tilde{\Omega}_{xy}$) is large. The contributions to the magnitude of the mean rate-of-rotation tensor is given in equation 7.

$$|2\tilde{\mathbf{\Omega}}|^2 = 2\tilde{\Omega}_{xy}^2 + 2\tilde{\Omega}_{xz}^2 + 2\tilde{\Omega}_{yz}^2 \tag{7}$$

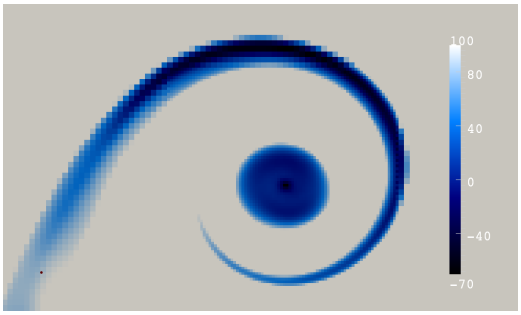

Figure 7: The corrected production term as a percentage of the original production term, shown at one chord length downstream of the tip of the wing in the traverse direction looking upstream.

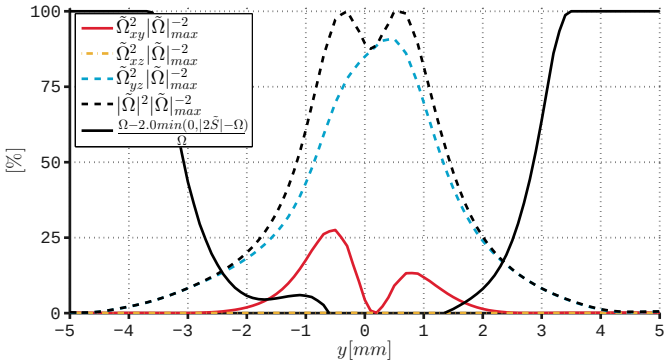

Figure 8: Contribution of the distinct term of the mean rate-of-rotation tensor to its magnitude and the damped production term of the SA-R model. The results are shown one chord length downstream of the wing tip looking downstream in the traverse direction over the horizontal axis.

4.5 Effects of the inclusion of transition

Experiments suggest [13] that the core radius is a function of the boundary layer thickness, as in equation 8. For a fully turbulent boundary layer the value $n = 0.2$, based on the turbulent boundary layer thickness formulation. In experiments a value of $n = 0.4$ has been found by McCormick, which is explained by the transitional boundary layer on the wing [14]. It is therefore expected that the viscous core radius is affected by the inclusion of transition in the turbulence model.

$$r_c \sim \delta_b \sim cRe^{-n} \tag{8}$$

The effect of transition on the growth of the viscous core and magnitude of the circulation within five viscous core radii at different locations downstream of the tip of the wing is shown in figure 9 and 10 respectively. It is observed that the circulation, normalized with the estimated circulation at the root (based on a lift coefficient of 0.71) of $\Gamma_0 = 0.24\frac{m^2}{s}$, is very similar to what is found in experiments on other section shapes with an elliptical planform [13]. The growth of the viscous core radius scales with $\sqrt{\nu_{app}t}$, where $t = \frac{x}{U_\infty}$, which is also shown with the estimated apparent viscosity of both cases in figure 9. The computation which includes transition produces better agreement with measurements.

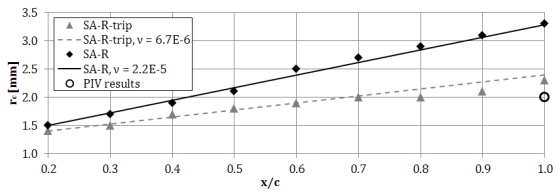

Figure 9: Growth of the radius of the viscous core size at different locations downstream of the tip of the wing. The lines give the approximated growth based on $\sqrt{\nu_{app}t}$ from $\frac{x}{c} = 0.2$.

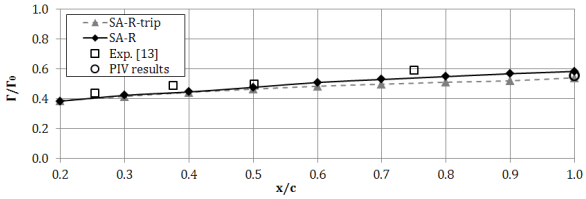

Figure 10: The circulation at different locations downstream of the tip of the wing, within five viscous core radii from the center of the vortex.

Further investigation of the turbulent viscosity in the roll-up region suggests a complex scaling of the viscous core radius. The boundary layer thickness and turbulent viscosity convecting from the wing are first affected by the shear layer forming in the wake of the wing. Then this shear layer enters the vortex in the roll-up process, where the high rotation begins to dampen the turbulent viscosity. This process is shown in figure 11 for both cases.

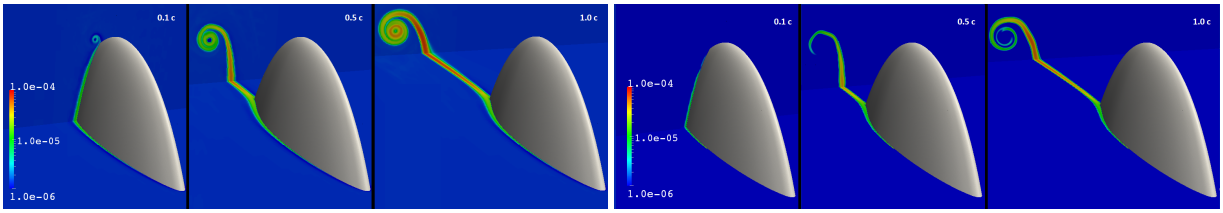

Figure 11: Turbulent viscosity in the roll-up region comparing the SA-R model on the left and the SA-R-trip model on the right. It is observed that the delayed transition decreases the turbulent viscosity significantly.

4.6 Effects of cavitation

When cavitation is introduced it is observed that the flow pattern in the vortex changes significantly. The circumferential velocity no longer follows the solid-body rotation profile as in the fully wetted flow. This is shown in figure 12, where also the PIV measurements for fully wetted flow are shown. There is a change in the velocity gradient close to the edge of the cavity, which might be related to the non-zero mass transfer in this region.

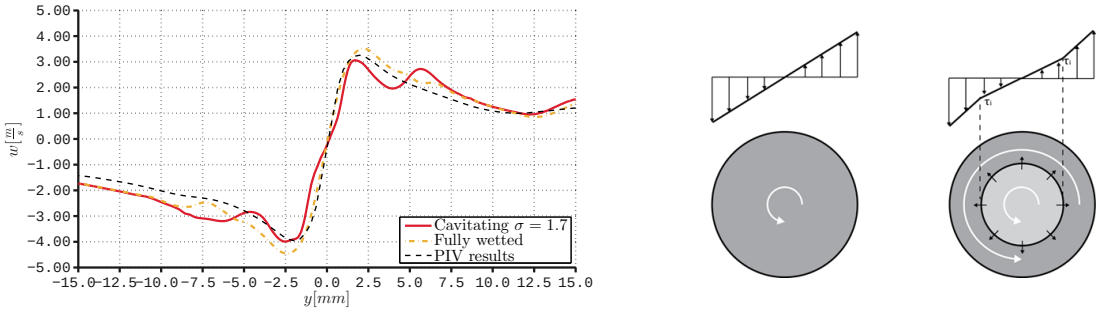

Figure 12: Circumferential velocity at one chord length behind the tip looking downstream in traverse direction over the horizontal axis. A schematic representation of the effect of cavitation is presented on the right, where a radial velocity resulting from local mass transfer is visible and a change in velocity gradient at the interface between the vapour and liquid.

Mass transfer leads to divergence of the velocity field as given in equation 9. The mass transfer is indicated with figure 14 where the red line gives the divergence of the velocity, which is non-zero near the edge of the cavity. The main contribution is found to be $\tilde{S}_{yy}$, which is the radial gradient of the radial velocity component. The largest components of the mean rate-of-strain tensor are shown in figure 13.

$$\nabla \cdot \tilde{U} = \left(\frac{1}{\rho_l} - \frac{1}{\rho_v}\right)\Gamma_l \tag{9}$$

$$\tilde{\boldsymbol{S}} = \frac{1}{2}\begin{bmatrix} \tilde{S}_{xx} & \tilde{S}_{xy} & \tilde{S}_{xz} \\ \tilde{S}_{yx} & \tilde{S}_{yy} & \tilde{S}_{yz} \\ \tilde{S}_{zx} & \tilde{S}_{zy} & \tilde{S}_{zz} \end{bmatrix} = \frac{1}{2}\begin{bmatrix} 2\frac{\partial u}{\partial x} & \frac{\partial u}{\partial y} + \frac{\partial v}{\partial x} & \frac{\partial u}{\partial z} + \frac{\partial w}{\partial x} \\ \frac{\partial v}{\partial x} + \frac{\partial u}{\partial y} & 2\frac{\partial v}{\partial y} & \frac{\partial v}{\partial z} + \frac{\partial w}{\partial y} \\ \frac{\partial w}{\partial x} + \frac{\partial u}{\partial z} & \frac{\partial w}{\partial y} + \frac{\partial v}{\partial z} & 2\frac{\partial w}{\partial z} \end{bmatrix} \tag{10}$$

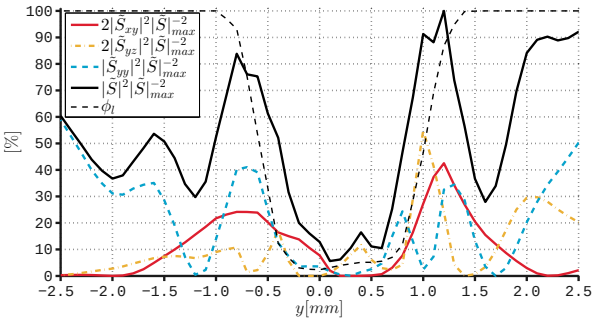

Figure 13: Magnitude of the rate-of-strain tensor, its largest components and the liquid fraction at one chord length downstream of the tip along the transverse horizontal line looking downstream.

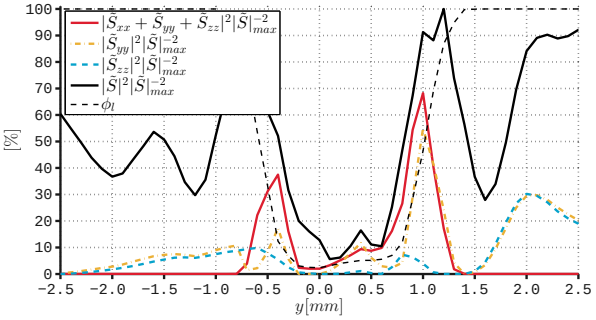

Figure 14: Magnitude of the rate-of-strain tensor, the components resulting from divergence of the velocity vector and the liquid fraction at one chord length downstream of the tip along the transverse horizontal line looking downstream.

In the viscous core the pressure reduction vanishes inside the cavity if present, which can be seen in figure 15. This is due to the low density of vapour compared to that of the liquid, as it decreases with a factor $6 \cdot 10^4$. The centrifugal component $-\rho\frac{u_\theta^2}{r}$ in the conservation of radial momentum (eqn. 11) is approximately balanced by the pressure gradient as shear and radial velocity are small in a solid-body rotation region. The centrifugal component is reduced due to the density difference.

$$\rho\Big(u_r\frac{\partial u_r}{\partial r} - \frac{u_\theta^2}{r}\Big) = -\frac{\partial p}{\partial r} + \mu\Big(\nabla^2 u_r - \frac{u_r}{r^2}\Big) \tag{11}$$

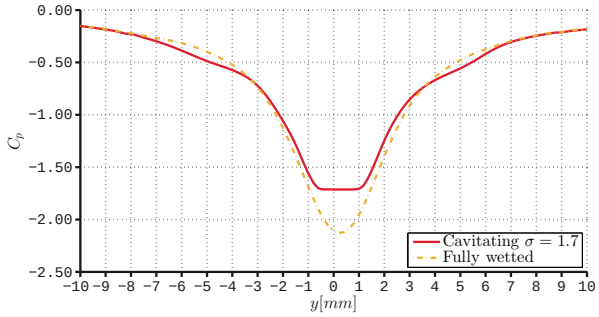

Figure 15: Pressure coefficient at one chord length behind the tip looking downstream along the horizontal axis.

The axial velocity in the core of a vortex is a result of the axial pressure gradient, which depends for a non-cavitating vortex on the growth of the core, gain in circulation in the roll-up process and effects of the boundary layer [15]. When cavitation is present the core pressure is very close to vapour pressure and the axial pressure gradient is therefore likely to be reduced in this region. This leads to the difference in the axial velocity

pattern shown in figure 16. It is however observed in both the PIV measurements and in experiments by [1] that the axial velocity is increased instead of decreased at this location. The difference is likely caused by numerical diffusion and the approximation within the rotations correction.

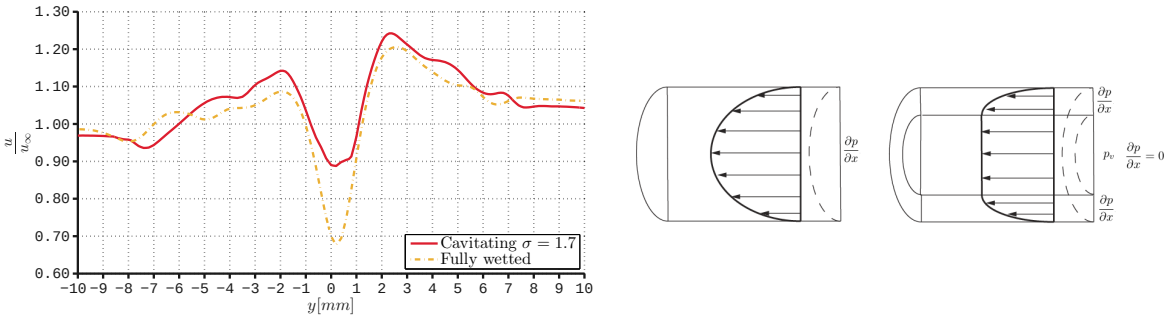

Figure 16: Axial velocity normalized by the free stream velocity at one chord length behind the tip looking downstream along the traverse horizontal line. A schematic representation of the effect of cavitation is presented on the right, where the reduction of the pressure gradient in the vapour core reduces the driving mechanism for the axial flow in that region.

5 CONCLUSIONS

The present study investigates the capabilities of OpenFOAM to predict steady tip vortex cavitation. It was found in a previous study that the simulation of a tip vortex flow with OpenFOAM is hampered by the numerical diffusion as a result of the second order accurate spatial discretisation [8]. This leads to an estimated numerical viscosity of the order of the fluid viscosity in the vortex.

The inclusion of the damping on the turbulence resulting from the high rotation in the vortex was necessary to avoid an excessive spreading of the vortex core. This correction reduces the turbulent viscosity to the same order as the fluid viscosity, making the numerical error and the amount of turbulence damping important for the prediction of the growth of the core.

Also the modelling of transition of the boundary layer affects the viscous core size of the vortex as a result of its turbulent viscosity rolling up in the vortex core. This is altered in the shear layer trailing the wing and damped when it rolls up in the vortex core.

It is concluded that for lower angles of attack laminar separation should be taken into account on this wing and that the empirical damping constant C_{rot} is not expected to mimic a physical damping rate. It is observed that the circumferential velocity profile, the core radius and circulation agree with the PIV measurements. However, the measured lift coefficient at the same conditions was significantly lower at about 0.56 affecting the strength of the vortex.

When cavitation is included in the simulation it is observed that the velocity profile of the vortex changes significantly. At the interface of the cavity there is mass transfer

and there is a change in circumferential velocity gradient present at this location in the solid-body rotation region. As a result of the large density difference of the water and vapour, the decrease in pressure is very small inside the vapour cavity. This likely leads to a reduction of the axial velocity in the vapour core of the vortex.

6 ACKNOWLEDGEMENTS

The developers of OpenFoam are gratefully acknowledged for making the CFD tool available. Furthermore, the Fluid Mechanics Section (FM) at the Laboratory for Aero & Hydrodynamics of the TU Delft is thanked for providing the resources for the computations.

LIST OF SYMBOLS

$\tilde{\boldsymbol{\Omega}}$	Mean rate-of-rotation tensor $\left(\frac{1}{2}\left(\nabla\tilde{U} - \nabla\tilde{U}^T\right)\right)$
$\tilde{\boldsymbol{S}}$	Mean rate-of-strain tensor $\left(\frac{1}{2}\left(\nabla\tilde{U} + \nabla\tilde{U}^T\right)\right)$
Δx	Local grid spacing
δ_b	Boundary layer thickness
Γ_l	Mass transfer rate of the liquid phase
ϕ_l	Liquid fraction
A_d	Area density $\left(\int_{-\infty}^{\infty} A_d dn = 1\right)$
b	Wingspan from tip to tip
c	Cord length
C_λ	Interface compression coefficient
C_{d_i}	Induced drag estimated with $C_{d_i} = \frac{C_L^2}{\pi AR}$
$C_{Langmuir}$	Mass transfer constant in the Langmuir evaporation equation
C_{rot}	Rotation constant of the SA-R model
Re	Reynolds number $\left(\frac{uL}{\nu}\right)$
y^+	Distance form the wall normalized by the viscous length scale

REFERENCES

[1] R. E. A. Arndt and A. P. Keller. Water Quality Effects on Cavitation Inception in a Trailing Vortex. *ASME*, Vol. **114**, 430–438, 1992.

[2] B. Maines and R. E. A. Arndt. The Case of the Singing Vortex. *J. Fluids Eng.*, Vol. **119**, 271–276, 1997.

[3] J. Bosschers. Investigation of the resonance frequency of a cavitating vortex. *NAG/DAGA, The Netherlands, Rotterdam*, 289–291, 2009.

[4] E. van Wijngaarden, J. Bosschers and G. Kuiper. Aspects of the cavitating propeller tip vortex as a source of inboard noise and vibration. *Proceedings of FEDSM2005, Houston, TX, USA*, 2005.

[5] S. S. Deshpande, L. Anumolu and M. Trujillo. Evaluation the performance of the two-phase flow solver inter-Foam. *Computational science & discovery*, Vol. **5**, 1–36, 2012.

[6] J. Dacles-Mariani, D. Kwak and G. Zilliac. On Numerical Errors and Turbulence Modeling in Tip Vortex Flow Prediction. *Int. J. Numer. Meth. Fluids*, Vol. **30**, 65-82, 1999.

[7] P. R. Spalart, S. R. Allmaras. A one-equation turbulence model for aerodynamic flows. *30th Aerospace sciences meeting & exhibit*, 1–22, 1992.

[8] J. J. A. Schot. *Numerical study of vortex cavitation on the elliptical Arndt foil*. M.Sc. Thesis. Technische Universiteit Delft: The Netherlands, 2014.

[9] ITTC. ITTC Recommended Procedures, Fresh Water and Seawater Properties. 2011.

[10] J. R. Cooper, R. B. Dooley. Revised Release on the IAPWS Industrial Formulation 1997 for the Thermodynamic Properties of Water and Steam. *The International Association for the Properties of Water and Steam*, 1997.

[11] R. E. A. Arndt, V. H. Arakeri and H. Higuchi. Some observations of tip-vortex cavitation. *Journal of fluid mechanics*, Vol. **229**, 269–289, 1991.

[12] J. S. Chow, G. G. Zilliac and P. Bradshaw. Turbulence measurements in the near-field of a wingtip vortex. *NASA TM*, 1997.

[13] J. A. Astolfi, D. H. Fruman and J. Y. Billard. A model for tip vortex roll-up in the near field region of three-dimensional foils and the prediction of cavitation onset. *European Journal of Mechanics - B/Fluids*, Vol. **18**, 757-775, 1999.

[14] B. H. Maines and R. E. A. Arndt. Tip vortex formation and cavitation. *Journal of fluid mechanics*, Vol. **119**, 413-419, 1997.

[15] G. K. Batchelor. Axial flow in trailing line vortices. *Journal of Fluid Mechanics*, Vol. **20**, 645–658, 1964.